Excitation power density dependence of a primary luminescent thermometer based on Er^{3+}, Yb^{3+}: $GdVO_4$ microcrystals operating in the visible

Nisrin Mohamed Bhiri [1,2], Mohamed Dammak [1], Joan Josep Carvajal [2], Magdalena Aguiló [2], Francesc Díaz [2] and Maria Cinta Pujol [2,*]

[1]Université de Sfax, Laboratoire de Physique Appliquée, Groupe de Physique des matériaux luminescents, Faculté des Sciences de Sfax, Département de Physique, BP 1171, Université de Sfax, 3018 SFAX, Tunisie, nesrine.bhiri@estudiants.urv.cat
[2]Universitat Rovira i Virgili, Departament de Química Física i Inorgànica, Física i Cristal·lografia de Materials i Nanomaterials (FiCMA-FiCNA) and EMaS,
Marcel·li Domingo 1, Tarragona, 43007, Spain
* Correspondence: mariacinta.pujol@urv.cat

Abstract

A discussion about the calibration of the Er^{3+},Yb^{3+}:$GdVO_4$ microcrystals as a luminescent primary thermometer based on the known equation of state of Boltzmann distribution of the electronic population of the two Erbium emitting coupled levels has been given. Its validity has been demonstrated. Besides, when Er^{3+},Yb^{3+}:$GdVO_4$ microcrystals acting as secondary thermometer, it has been proven the dependence of the thermometric ratio based on the integrated intensities of the green visible emissions arising from the two thermally coupled levels of erbium, $^2H_{11/2}$ and $^4S_{3/2}$, on the excitation power density for the Er^{3+},Yb^{3+}:$GdVO_4$ microcrystals. The effect of the excitation power density on the relative thermal sensitivity and temperature resolution has been also analyzed.

Keywords: luminescent thermometer, primary thermometer, Er^{3+},Yb^{3+}:$GdVO_4$, excitation power density, laser heating.

1. Introduction

The necessity of novel systems for measuring the temperature by non-contact or semi-non-contact techniques in systems with dimensions in the micron, sub-micron, and nanometer scale has provoked an intense research in the last years for developing novel nano or micro thermometers. Luminescent thermometers based on the spectral analysis of the emission that changes with temperature is particularly interesting to determine a thermal detection. Lanthanide-doped materials offer some attractive features to be used as nano or micro thermometers, such as the small dimensions, chemical and physical stability, versatility in the wavelengths used for excitation and for reading the temperature through the light emitted by these particles, and the relatively high thermal sensitivity that can be achieved with these systems, allowing for a thermal resolution below 1 K [1]. On the other hand, some attention should be paid to their reliability when used as luminescent thermometers, as indicated by Labradoz *et al.* [2], related to the effect of the excitation power in their performance, and/or the effects related to the self-absorption of the emitted light. Very good and recent reviews dealing with luminescence thermometry based on lanthanide-doped crystals can be found in the current literature [3,4].

A classical approach for determining the temperature based on the photoluminescence of the lanthanide ions is the use, as thermometric parameter, Δ, of the ratio between two emission intensities, $\frac{I_2}{I_1}$, using their integrated intensity (known also as FIR, fluorescence intensity ratio). If these two emitting levels (1 and 2) are close enough energetically to be thermally coupled (200-2000 cm^{-1} [5]), the Boltzmann distribution law will determine the electronic population distribution among them, and then, the temperature can be determined from:

$$\Delta = \frac{I_2}{I_1} = \frac{g_2 \vartheta_2 A_2}{g_1 \vartheta_1 A_1} exp\left(\frac{-\Delta E}{k_B T}\right) = Bexp\left(\frac{-\Delta E}{k_B T}\right) \tag{1}$$

being I_2 and I_1, the two integrated intensities for the electronic transitions from levels 2 and 1 to the ground state, respectively, g_2 and g_1 are the degeneracy of the two emitting levels, when using the

Er^{3+} ion being the $^2H_{11/2}$ and $^4S_{3/2}$ levels, respectively; ν_2, ν_1, A_2 and A_1 are the frequencies and spontaneous emission rates corresponding to these levels, respectively; k_B is the Boltzmann constant, and ΔE is the difference of energy between the barycenter of the two emitting thermally coupled levels (TCLs). B is the pre-factor constant, which depends on radiative parameters of the emitting ion, such as the degeneracy of the emitting levels, their branching ratio to the ground state and the spontaneous emission rates of their emissions to the ground state, and the angular frequencies, related to the wavelength of emission, of the two emissions [3].

The ΔE and the B parameters could be determined by fitting the FIR data and its dependence with the temperature in single-center thermometers based on the FIR TCLs. In this cases, an external calibration of the thermometric parameter is needed; and typically, this calibration procedure requires measuring the temperature using a thermocouple. This allows the obtaining of the intensity-to-temperature conversion. In 2017, Balabhadra *et al.* [6] in 2017 demonstrated that single-center thermometers based on two TCLs are intrinsically primary thermometers, because ΔE and the B parameters could be measured independently of any calibration. Also, in Balabhadra *et al.* [6] in 2017, classified for the first time the luminescent thermometers, as primary and secondary, in relation with their calibration procedure: primary thermometers are characterized by an equation of state that relates a particular measured value to the absolute temperature without the need of calibration; and secondary thermometers, when previous calibration is needed.

If the equation of state used is the one related to the Boltzman equation (Eq. 1), it is needed to determine ΔE and B independently of the temperature, in order to obtain the equation of state of our system, and use it as the relationship between the temperature and the thermometric parameter.

Primary thermometers could be an alternative to the usual calibration procedures in a secondary thermometer requiring an independent measurement of the temperature (using, for instance, a thermocouple or an infrared camera) to obtain the corresponding relationship between the thermometric parameter and the temperature, and further calibration procedures needed if the thermometer operates in different media. As mentioned by them, to develop and understand effective luminescent primary thermometers in which the thermometric ratio is based on a known equation of state, would avoid the time-consuming tasks of multiple calibration in different mediums. Furthermore, as Brites *et al.* [7] commented any upconverting thermometer based on thermally-coupled energy levels is intrinsically a primary thermometer governed by an equation of state expressed as that in Eq.1.

Then, thermometers based on Eq. (1) are intrinsically primary thermometers and, therefore, this equation is used as temperature calibration independently of the medium [1,6,8,9]. The ΔE value could be by an envelope fitting to the I_1 and I_2 spectra [10]; and the B_0 parameter is empirically deduced from the plot of Δ depending on the laser excitation power density extrapolating the data to the zero excitation power density [1,6]. When the laser-induced heating is negligible (i.e. zero excitation power density), the temperature T_0 corresponds to the room temperature [11,12] and the thermometric parameter, at zero excitation power density Δ_0, is given by:

$$\Delta_0 = B_0 exp\left(\frac{-\Delta E}{k_B T_0}\right) \qquad (2)$$

So, using expression (2), the B_0 can be calculated.

A good candidate to be used as lanthanide doping ion for thermometric applications is the Er^{3+} ion, used in a host that allows having a unique crystalline site, and then used as single-emitting center. In Er^{3+}, often, the thermometric ratio is given using the emissions originated from the $^2H_{11/2}$ and $^4S_{3/2}$ TCLs, which emit intense green light when decaying radiative to the ground state. Therefore, traditionally, the approach described above using Eq. (1) has been applied to the Er^{3+} ion [3]. Besides, due to the facility of this ion to present up-conversion (UC) when it is sensitized with Yb^{3+}, the couple of Yb^{3+} and Er^{3+} ions has been extensively used to be excited around 980 nm and using the green emissions for reading the temperature, based in their efficient UC sensitized process [11].

There are few works in the literature in which they developed primary luminescent thermometers. The first work of Balabhadra *et al.* in 2017 [6] already reported the possibility to use as a luminescent primary thermometer, a thermometer based on the UC process of the emission of Er^{3+} TCLs in Er^{3+},Yb^{3+} co-doped SrF_2 nanocrystals. Later on, Brites *et al.* [7] combined a primary thermometer and a secondary thermometer creating a self-referenced double thermometer, based on Ln^{3+}-doped $NaYF_4$ and $NaGdF_4$ nanoparticles (Ln = Yb, Er, Tm) embedded in two PMMA films. The primary thermometer was based on the $^2H_{11/2} \rightarrow {}^4I_{15/2}$ and $^4S_{3/2} \rightarrow {}^4I_{15/2}$ Er^{3+} transitions, while the secondary thermometer was based on the temperature dependence of a ratio of intensities. The maximum relative thermal sensitivity of the thermometer was $2.96\%\cdot K^{-1}$ and the minimum temperature uncertainty was 0.07K (both at 300K), with the maximum S_r value corresponding to a 2.3-fold improvement, with respect to the previous referred Er^{3+}-based primary thermometer. It is also worth to mention that Botas *et al.* [A.M.P. Botas, C.D.S. Brites, J. Wu, U. Kortshagen, R.N. Pereira, L. D. Carlos and R. A. S. Ferreira, Part. Part. Syst. Charact. 2016, 33, 740–748] previously in 2016, used another equation of state to develop a luminescent primary thermometer. In that case the temperature dependence of the emission peak position of Si NPs, used as the thermometric parameter, was well-described by the Varshni's law, enabling the development of a primary thermometer. The thermometer showed a maximum relative sensitivity of $0.04\%\ K^{-1}$.

On the other hand, several works [14,15] have already reported and illustrated the important variation of the thermometric ratio on the excitation power density in different crystalline host used as a base for the thermometer, that continuously decreases with the increment of excitation power density. Other host seems that do not exhibit this dependence [15]. Two different effects can contribute to this dependence, such as the laser heating effect on the sample and the different dependence of the electronic population of the two emitting levels with the temperature, in which the luminescent thermometer will be based on the laser power density. However, for the moment there are no reports on the influence of the excitation power on the performance of a luminescent primary thermometer.

In the present work, we will evaluate the characteristics of the calibration of a primary thermometer based on Er,Yb:$GdVO_4$ microcrystals (MCs) with the effects induced by the different excitation powers. We have studied a specific doping concentration, 1 at. % Er^{3+}, 20 at. % Yb^{3+} co-doped $GdVO_4$, which was observed in a previous work as the chemical composition which provided the best thermometric performance [18].

2. Materials and Methods

Microcrystals of 1 at. % Er^{3+}, 20 at. % Yb^{3+} co-doped $GdVO_4$ (1 and 20 being the atomic substitution of Gd^{3+} ion by Er^{3+} and Yb^{3+} ions, respectively) were synthesized by high temperature solid-state reaction, as reported previously [18]. Briefly, we used as starting precursors the commercial compounds: NH_4VO_3 (analytical), Gd_2O_3 (99.99 %), Er_2O_3 (99.99 %) and Yb_2O_3 (99.99 %). These compounds were weigthed in stoichiometric proportions; mixed and then, grounded manually in an agate mortar. The mixture was calcinated at 1173 K for 6 h in a conventional oven to obtain the Er^{3+},Yb^{3+}: $GdVO_4$ MCs.

X-ray powder diffraction was used for identifying the crystalline structure of the as prepared powders using a Bruker AXS D-8 Advance diffractometer equipped with a Cu Kα radiation source (λ = 1.5406 Å), with operation parameters such as 40 kV and 40 mA.

Morphologies of the MCs were observed with an environmental scanning electron microscopy (ESEM, FEI QUANTA 600).

The Raman spectrum was measured using a Labram HR800 UV Raman spectrometer from Horiba-Jobin-Yvon. The excitation was carried out with a visible (Vis) argon laser operating at 514 nm using a 50X Vis microscope objective with 0.5 numerical aperture.

For the photoluminescence studies of the microcrystals, they were excited by a 980 nm fiber-coupled diode laser and the beam was focused on the sample using a 20X microscope objective (numerical aperture 0.4). The emission spectra were recorded in a Yokogawa AQ6373 optical spectrum analyzer, with a resolution of 10 nm and an integration time of 1 s for the room temperature emission spectra and with a resolution of 2 nm and an integration time of 10 s for the temperature dependent emission spectra. The scattered excitation radiation was eliminated by using a 750 nm short pass dichroic filter (Thorlabs). For the temperature-photoluminescence measurements, the MCs were placed in a heating stage (Linkam, THMS 600) in which the temperature is measured by a temperature sensor with a 0.1 K resolution.

3. Results

3.1. Microcrystals characterization

A careful study of the obtained MCs was published in Bhiri *et al.* [18]. Briefly, the obtained microparticles crystallize as a single crystalline structure, as observed in the X-ray powder pattern presented in Fig. 1a. They belong to the tetragonal crystalline phase, $I4_1/amd$ space group (unit cell parameters a = 7.21 Å and c = 6.34 Å given in JCPDS 017-0260 [19]). Fig. 1b shows an ESEM image of the obtained microparticles, showing grains with sizes in the micrometer range distributed in a heterogeneous way.

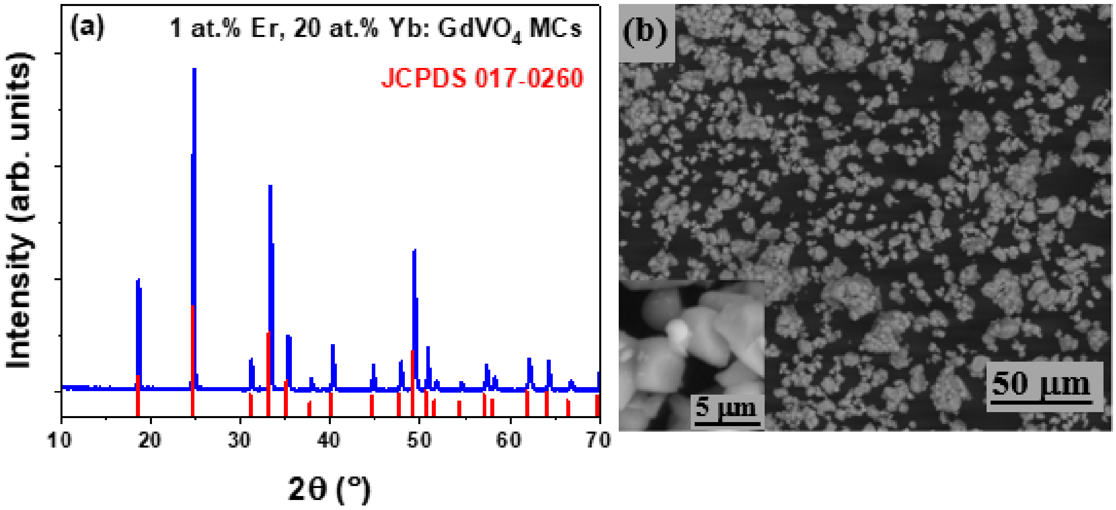

Fig. 1. (a) X-ray diffraction patterns of Er^{3+},Yb^{3+}: $GdVO_4$ MCs synthesized by the solid-state reaction method. The standard XRPD pattern, corresponding to $GdVO_4$ (JCPDS data, PDF card No. 017-0260) was included for comparison. (b) ESEM image of the as obtained Er^{3+},Yb^{3+}: $GdVO_4$ MCs.

Due to the importance of the non-radiative mechanisms in the discussion of this paper, especially because of the multiphonon non-radiative decay paths, it is also worth to summarize here the energy phonon values of the $GdVO_4$ host. As also reported in Bhiri *et al.* [18], an energy band observed at around 740 cm^{-1} is attributed to the infrared (IR) active phonon mode assigned to the v_3 VO_4^{3-} stretching vibration band [20]. Fig. 2 shows the Raman spectrum of Er^{3+},Yb^{3+}: $GdVO_4$ MCs where the internal and external vibrational modes of $[VO_4]^{-3}$ in $GdVO_4$ phase have been identified. In the external vibrational modes, four peaks are observed in the range of 100−300 cm^{-1} [21,22]. The peak at 374 cm^{-1} corresponds to the symmetric bending δ_s (VO_4) mode, whereas the peak at 479 cm^{-1} corresponds to the asymmetric deformation δ_{as} (VO_4) mode. The peaks at 806 and 821 cm^{-1} correspond to the asymmetric stretching v_{as} (VO_4) mode. Besides, the largest Raman active phonon value for this host is observed at around 882 cm^{-1} attributed to the symmetric stretching v_s (VO_4) vibration mode [23,24]. So, these large phonon values can be related to the importance of the role of the multiphonon non-radiative decays observed in this host. If we compare with the phonon energy values reported for the largely used hosts in UC thermometers, such as $NaYF_4$, in which the average largest Raman phonon value is 360 cm^{-1} [25], the one of our sample is much larger than it. For Er^{3+} based thermometers, other oxide hosts, as $CaWO_4$ with phonon values about to 912 cm^{-1} [26], it is slightly larger than the one of vanadates.

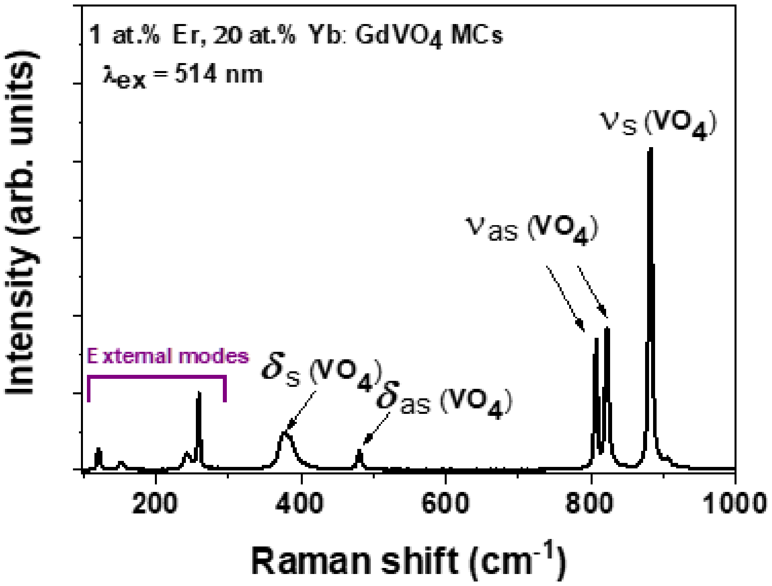

Fig. 2. Raman spectrum of Er^{3+},Yb^{3+}: $GdVO_4$ MCs synthesized by the solid-state reaction method.

3.2. Primary thermometer

Using a single emission center, as source of the ratio of the emission intensities of two distinct transitions, used as the thermal sensing parameter, and using the Er^{3+} green emissions to obtain this ratio, the ratio of fluorescence intensities, Δ, known also as FIR (fluorescence intensity ratio), can be described as:

$$\Delta = \frac{I_H}{I_S} = \frac{g_H \vartheta_H A_H}{g_S \vartheta_S A_S} exp\left(-\frac{\Delta E}{k_B T}\right) = Bexp\left(-\frac{\Delta E}{k_B T}\right) \tag{3}$$

being I_H and I_S, the integrated intensity of the two green emissions arising from the $^2H_{11/2}$ and $^4S_{3/2}$ emitting levels, respectively, from Er^{3+} ion; g_H and g_S are the degeneracy of the $^2H_{11/2}$ and $^4S_{3/2}$ levels, respectively; ν_H, ν_S, A_H and A_S are the frequencies and spontaneous emission rates corresponding to these levels; B is the pre-exponential constant; ΔE is the energy gap between the $^2H_{11/2}$ and $^4S_{3/2}$ levels in the particular host ($GdVO_4$ in this case); k_B is the Boltzmann's constant and T is the absolute temperature. Then, the absolute temperature can be determined as:

$$T = \frac{\Delta E}{k_B} \frac{1}{\ln(\frac{B}{\Delta})} \tag{4}$$

Fig. 3 shows the room temperature photoluminescence UC emission spectra in the 490 to 580 nm range for 1 at. % Er^{3+}, 20 at. % Yb^{3+}: $GdVO_4$ MCs excited at 980 nm under different laser power density excitations ranging from 23 to 463 W cm^{-2},

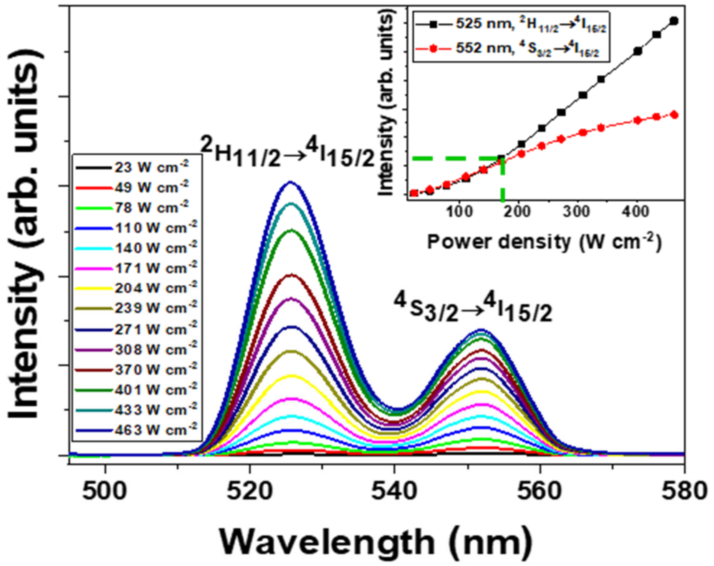

Fig. 3. Excitation laser power density dependent room temperature UC emission spectra for 1 at.% Er^{3+}, 20 at.% Yb^{3+}: $GdVO_4$ MCs.

These spectra exhibit two strong emission bands located in the green visible region, which come from the $^2H_{11/2}\rightarrow ^4I_{15/2}$ (~525 nm) and $^4S_{3/2}\rightarrow ^4I_{15/2}$ (~552 nm) electronic transitions of Er^{3+} ions. As shown in Fig. 3, the UC luminescence of the analyzed sample can be seen even at low laser excitation power densities (23 W cm^{-2}) and its intensity increases significantly as the excitation laser power density increases, which can be correlated to the increasing electronic populations in the excited states of the doping ions induced by the optical excitation. It is worth noting also that up to 463 W cm^{-2}, the intensity of the emission peaks remains increasing. For thermometry study, as demonstrated by Marciniak et *al.* [27], upon higher excitation power density the increase of the sample temperature does not lead to changes of the $^2H_{11/2}$ state according to the Boltzmann distribution law then it is not necessary to go up for higher values. Below an excitation laser power density of 171 W cm^{-2}, the intensity of the emission attributed to the $^4S_{3/2}\rightarrow ^4I_{15/2}$ transition is slightly stronger than that of the $^2H_{11/2}\rightarrow ^4I_{15/2}$ transition. At 171 W cm^{-2}, however, the emission intensities coming from the two manifolds are almost the same, while, above this value the intensity of the $^2H_{11/2}\rightarrow ^4I_{15/2}$ transition become stronger than that of the $^4S_{3/2}\rightarrow ^4I_{15/2}$ transition (see the inset in Fig. 3).

Theoretically, the energy gap ΔE does not depend on the excitation laser power density, and then the energy gap should be the same whatever the value of the excitation laser power density used. The experimental energy gap ΔE between the two manifolds ($^2H_{11/2}$ and $^4S_{3/2}$) can be extracted by fitting the two peaks to a Gaussian function (I_H and I_S) in the experimental photoluminescence spectra recorded at room temperature (300 K) and at different excitation laser power density values, and then by calculating the energy separation between the barycenters of the $^2H_{11/2}$ and $^4S_{3/2}$ levels. The variation of the ΔE with the excitation laser power density for the 1 at. % Er^{3+}, 20 at. % Yb^{3+}:$GdVO_4$ MCs are summarized in Table 1. As expected, all the values are very similar due to the shielding of the active electrons in the lanthanide ions in relation of the crystal field, remaining always in the 893-916 cm^{-1} range (see Fig. SI 1). The closest value of the energy gap to the theoretical one (785 cm^{-1}) [28] corresponds to the minimum value (893 cm^{-1} ± 6 cm^{-1}, error determined directly from the Gaussian fit of each spectrum) obtained at 49 W cm^{-2}.

Fig. 4 shows the evolution of Δ at room temperature (300 K) in relation with the excitation laser power density. The most feasible mechanism responsible for the increase of Δ as the excitation laser power density increases is the increasing significance of the non-radiative mechanisms populating the $^2H_{11/2}$ energy level, so then, the thermalization process. Other mechanisms reported in the literature for this increase, like the contribution of other transitions to the green emission at high excitation laser power densities ($^2P_{3/2}\rightarrow ^4I_{9/2}$, for instance [29]) have been disregarded since no additional peaks have been observed in the spectra obtained in the excitation power density range explored (see Fig. 7).

The value of Δ at no-laser excitation (no laser-heating) labeled as Δ_0 and the corresponding *B* pre-exponential factor can be determined from the plot of Δ vs the excitation laser power density by extrapolating the linear fit to the limit of zero excitation laser power density (see Fig. 4). As observed in Fig. 4, the linear behavior can be extended till a laser excitation power density of 329 W cm^{-2} in the sample and set-up used. In the literature, it has been reported that the linear behavior for the Er-Yb systems can be expected in the range of 100-300 W cm^{-2} [1]. At high excitation power densities, the dependency of Δ is not linear any more, because Δ is not only governed by the Boltzmann law as responsible for the electronic population of the two emitting states, but non-radiative depopulation mechanisms become important [27].

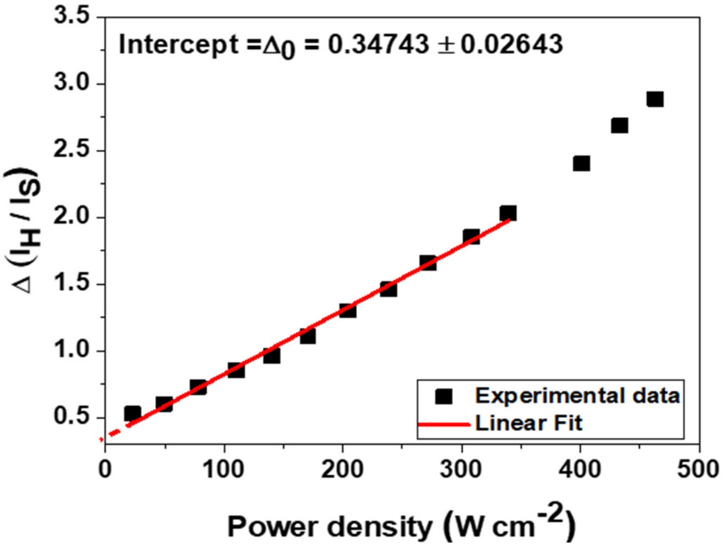

Fig. 4. Thermometric parameter dependence with the excitation laser power density for the 1 at. % Er^{3+}, 20 at.% Yb^{3+}: $GdVO_4$ MCs, measurements performed at room temperature.

The intercept corresponding to the Δ_0 value is 0.35± 0.03. Using Eq. (3) with $\Delta = \Delta_0$, $T = 300$ K and ΔE as 893 cm^{-1}, the *B* parameter could be calculated as 25.2. This value is very close to the one calculated using the Judd Ofelt parameters and the expression reported by Brites *et al.* [30], being 26.4 reported in our previous work [18]. In the Erbium coupled levels, there's a correspondence between the B pre-exponential factor with the three intensity Judd Ofelt parameters Ω_2, Ω_4 and Ω_6 which is related to the fact that the radiative probability can be calculated as a function of the Judd-Ofelt parameters; and the ratio of intensities is related to the ratio of the radiative transition rate of each transitions. Summarising, the primary thermometer can be described with the equation $\Delta = 25.2 exp\left(-\frac{893}{k_B T}\right)$.

3.3. Dependence of the measured temperature with the excitation laser power density

Once these parameters are determined, the temperature can be calculated from the Δ/Δ_0 ratio, being the Δ the experimental thermometric variable, using the following equation derived from the combination of Eq. (3) and Eq. (4) as a primary thermometer:

$$\frac{1}{T} = \frac{1}{T_0} - \frac{k_B}{\Delta E}\ln\left(\frac{\Delta}{\Delta_0}\right) \tag{5}$$

In order to calculate the temperature, which will be noted from now on by T_{abs}, using Eq. (5), we present in Fig. 5 its variation with the temperature reading using a thermocouple, T_{mes}, placed in contact with the sample holder of the 1 at. % Er^{3+}, 20 at. % Yb^{3+}: $GdVO_4$ MCs excited at 980 nm with different excitation powers from 7 mW to 103.8 mW. The Δ the experimental thermometric variable is extracted from the data of the Fig. 8.

Closer to room temperature, we can see that there is a significant difference between the calculated absolute temperature and the one measured with the thermocouple for all the excitation laser power densities used, such as, for all their values,~~ we are underestimating the temperature with the primary thermometer.~~ When the temperature of the sample increases, this difference is reduced until the two values become identical at 480 K and above for the lower excitation laser power density used (23 W cm^{-2}). However, for higher excitation laser power densities, this difference remains almost the same, with the tendencies observed running almost parallel to the temperature determined at the limit of zero laser excitation power density. That can reflect the effect of the sample heating generated at higher excitation laser power densities. Particularly, when we used a laser excitation power density of 23 W cm^{-2}, the difference between T_{abs} and T_{mes} should be due to the local increment of the particles' temperature induced by the laser excitation. Similar behavior has been already reported by Balabhadra *et al.* [6].

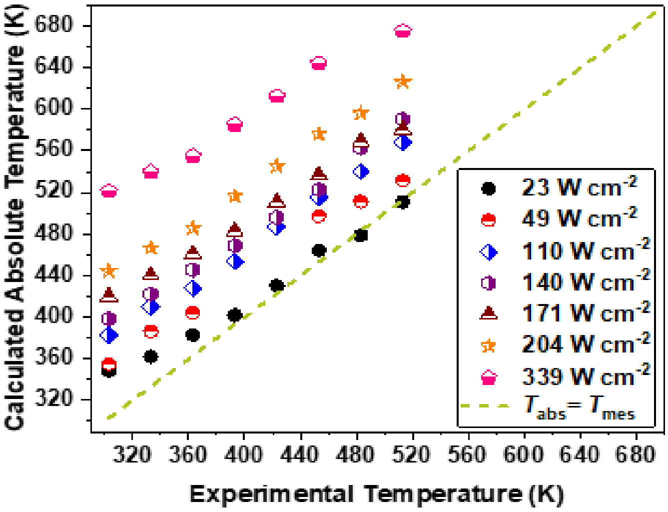

Fig. 5. Calculated absolute temperature, T_{abs}, using Eq. (5) with T_0 = 299.9 and Δ_0 = 0.035, ΔE is the experimental energy gap obtained at room temperature (300 K) for each given excitation laser power density (23 W cm^{-2} – 339 W cm^{-2}) *vs* the experimental temperature measured, T_{mes}, with a thermocouple for the 1 at.% Er^{3+}, 20 at.% Yb^{3+}: $GdVO_4$ MCs. The dashed line corresponds to $T_{abs} = T_{mes}$.

Applying Eq. (5), the absolute temperature, T_{cal}, can be determined at different excitation power densities in the 23-339 W cm^{-2} range for the analyzed sample, being that T_0 = 299.9 K, ΔE = 893 cm^{-1} and Δ_0 = 0.35 are the parameters corresponding to no laser-induced heating, and Δ represents the ratio of I_H to I_S determined at a given temperature of 303 K and at different excitation laser power densities (using the photoluminescence emission spectra taken at 303 K and showed in Fig. 8). Fig. 6 show these determined absolute temperatures~~, T_{cal},~~ at different excitation laser power densities when the temperature was 303 K. It can be seen that when increasing the excitation laser power density values, the extra heating of the sample induced by the laser makes the T_{cal} larger than the measured temperature by the thermocouple. Using the expression $\Delta T = T_{cal} - T_{mea}$, where T_{cal} represents the absolute temperature determined with the luminescent thermometer, and T_{mea} represents the temperature read using a thermocouple (303 K), the Δtemperature was determined, as depicted in the bottom panel in Fig. 6. It can be seen that the local temperature increases from 348 K to 521 K on increasing the excitation laser power density from 23 W cm^{-2} to 339 W cm^{-2}. A similar behavior was observed in 1% Ho, 10% Yb: $CaWO_4$ for the two TCLs of Ho^{3+} ion [31].

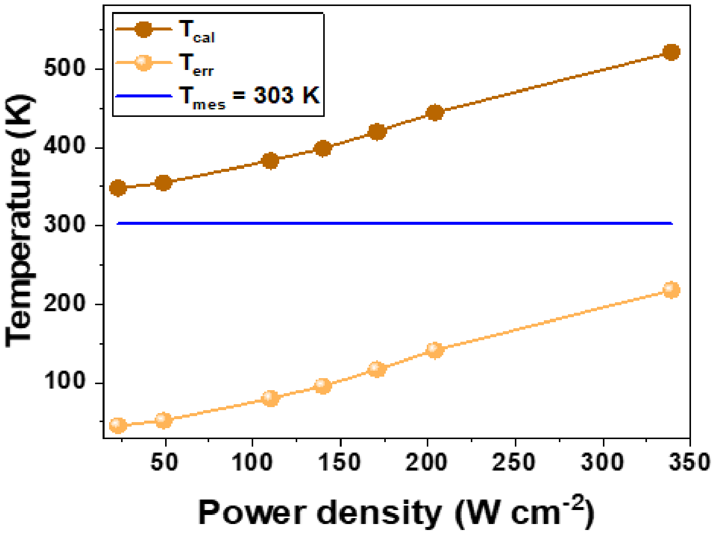

Fig. 6. Absolute temperature determined with the luminescent thermometer, T_{cal}, and ΔT as a function of the excitation laser power density for the 1 at. % Er^{3+}, 20 at.% Yb^{3+}: $GdVO_4$ analyzed sample when the real temperature, measured with a thermocouple, was kept constant at 303 K.

3.4. Dependence of the thermometric ratio with the excitation laser power density

As mentioned in the introduction, when the power dependence of the emission arising from the $^2H_{11/2}$ level versus the emission arising from the $^4S_{3/2}$ level is different, it indicates that there is a dependence of the FIR with the excitation power density [15]. Fig. 7 a shows the power density dependence of these two emissions in our sample. As mentioned in Li *et al.* [16], for a non-saturated UC process, the UC emission intensity I is proportional to the excitation laser power P, i.e., $I \propto P^n$, where n is the number of photons necessary for populating the corresponding emitting excited state. So, regarding to the results plot in Fig. 7a the slopes at lower excitation power densities, below 204 W cm^{-2}, are almost similar for both emissions and the number of photons required for populating the $^2H_{11/2}$ and $^4S_{3/2}$ levels in our sample are n_{low} = 2. However, at higher excitation laser power densities, above 204 W cm^{-2}, the slopes, n_{high}, for the two $^2H_{11/2}$ and $^4S_{3/2}$ levels diverge. Above this value the saturation regime is reached for the emission arising from the $^4S_{3/2}$ level, while, apparently, the saturation regime for the emission arising from the $^2H_{11/2}$ level occurs at higher excitation power densities, not reached in this study. Nevertheless, since the saturation regime is reached for one of the emissions considered for FIR, it is not necessary to analyse the limit value for the other. The large difference in the slopes at higher excitation laser power densities might be a consequence of the effect on the UC intensity dependence by the heating of the sample caused by the laser excitation [32], but also, by the different competition between the linear decay and the UC processes for each emitting state [33]. Indeed, due to the complexity of the energy level structure of the lanthanide ions, the excited states can be populated and depopulated via several different channels. These complex electronic populating mechanisms and the competition between the linear decay and the UC processes affect to the dependence between the FIR and the excitation laser power densities, deviating it from the theoretical number of photons required to achieve the population of the excited state [16].

The energy transfer (ET) mechanism from Yb^{3+} ion to Er^{3+} ion by a 980 nm UC excitation has already been explained in detail in our previous work [18], through which, Yb^{3+} ions can efficiently transfer their energy to Er^{3+} [34], populating its $^4I_{11/2}$ excited state. The excited Er^{3+} $^4I_{11/2}$ electronic state can get the energy from a second surrounding Yb^{3+} ion and promote its electrons to the $^4F_{7/2}$ higher energy level. Then, the Er^{3+} ion in its $^4F_{7/2}$ excited state can be de-excited non-radiatively to the $^2H_{11/2}$ and $^4S_{3/2}$ excited states. From there, the radiative relaxations to the ground state produce the green emissions (see Fig. 6b). Therefore, it is quite clear that these emissions are mainly a two-photon UC process, as already deduced from the calculation of the n value.

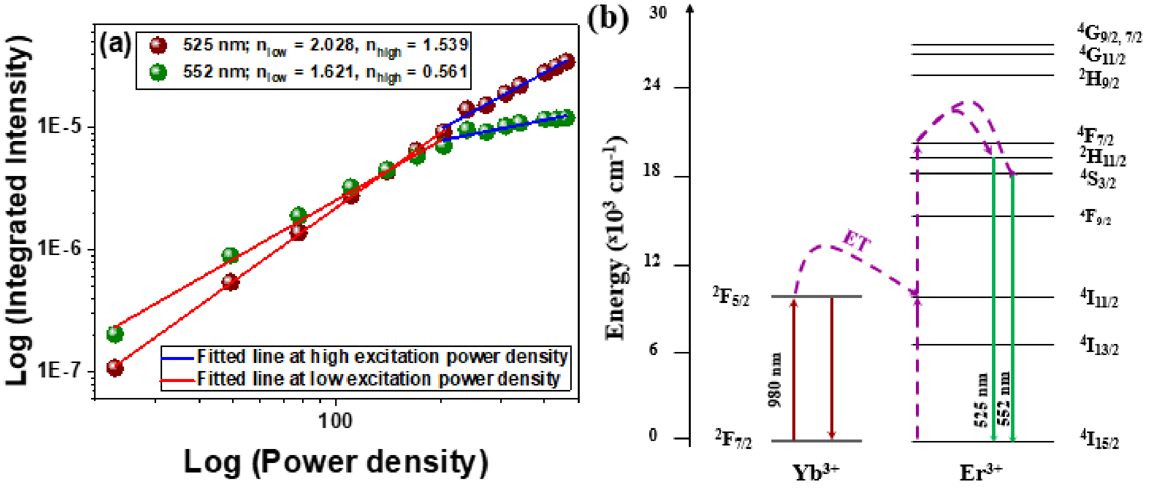

Fig. 7. (a) Excitation laser power density dependence of the green emission intensities arising from the two $^2H_{11/2}$ and $^4S_{3/2}$ levels for the 1 at.% Er^{3+}, 20 at.% Yb^{3+}: GdVO$_4$ MCs excited at 980 nm; linear fittings corresponds to the equation $I \propto P^n$, n_{low} and n_{high} corresponds to the slopes at low and high excitation laser power densities, respectively. (b) Energy level diagram of the Er^{3+}-Yb^{3+} system in GdVO$_4$ and feasible UC mechanisms under near-infrared (980 nm) excitation.

In order to analyze the effect of the excitation laser power density values on the FIR-based luminescent thermometer in 1 at. % Er^{3+}, 20 at. % Yb^{3+}: GdVO$_4$ MCs operated under UC, the dependence of their emission spectra was measured at different excitation laser powers, from 23 W cm^{-2} to 339 W cm^{-2}, in the 303 - 513 K temperature range (see Fig. 8). All the spectra show two green bands corresponding to the transitions from the $^2H_{11/2}$ and $^4S_{3/2}$ excited-state levels to the $^4I_{15/2}$ Er^{3+} ground state. At low temperatures and at low excitation laser power densities (below 204 W cm^{-2}) the intensity of the emission band coming from the $^4S_{3/2} \rightarrow {}^4I_{15/2}$ transition was stronger than that of the $^2H_{11/2} \rightarrow {}^4I_{15/2}$ transition. When the temperature increased, the emission intensity of the $^2H_{11/2} \rightarrow {}^4I_{15/2}$ transition became stronger than that of the $^4S_{3/2} \rightarrow {}^4I_{15/2}$ transition. Also, for excitation power densities above 204 W cm^{-2}, the emission arising from the $^4S_{3/2}$ manifold became weaker than that arising from the $^2H_{11/2}$ manifold even at low temperatures, indicating that above this excitation laser power density value we reached the saturation regime. Taking into account the discussion given by Marciniak *et al.* [27], as a consequence, a decrease of the thermometric performance should be observed.

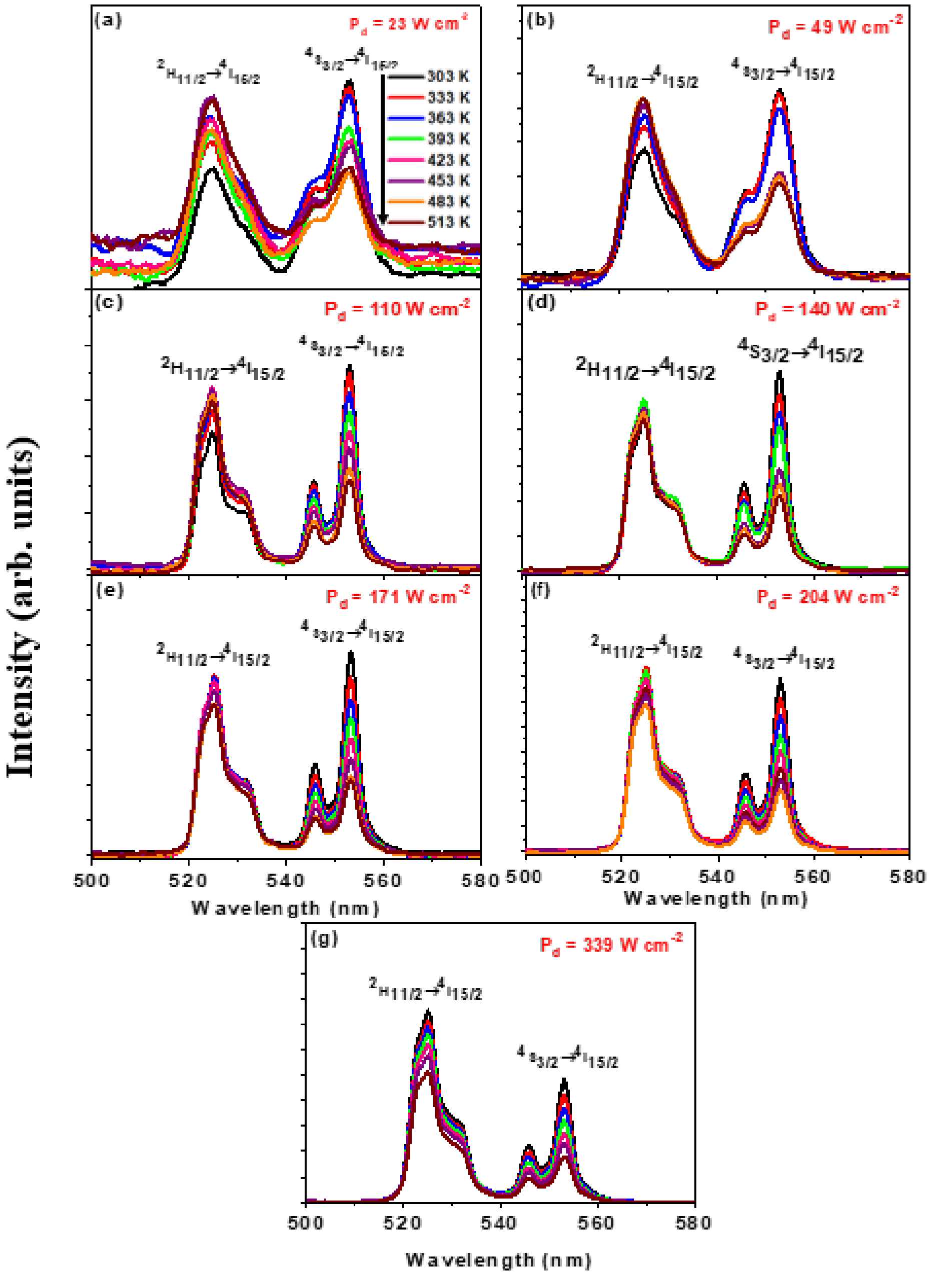

Fig. 8. Temperature dependent UC emission spectra of 1 at. % Er^{3+}, 20 at.% Yb^{3+}: $GdVO_4$ MCs measured in the 303-513 K temperature range and excited under 980 nm different excitation laser power densities: (a) 23 W cm^{-2}, (b) 49 W cm^{-2}, (c) 110 W cm^{-2}, (d) 140 W cm^{-2}, (e) 171 W cm^{-2}, (f) 204 W cm^{-2} and (g) 339 W cm^{-2}.

The thermometric parameter (FIR), Δ, for each spectrum has been calculated by integrating the areas for each manifold, for each temperature and each excitation laser power density. The evolution of Δ obtained at different excitation laser power densities and different temperatures is depicted in Fig. 9. As expected by the different n values obtained in Fig. 7, there is an important dependency of Δ with the excitation laser power density. A similar behavior was observed in Er,Yb: $CaWO_4$ phosphors [16]. However, other results reported for 1 at. % Er, 5 at % Yb doped $BaMoO_4$ nanoparticles show no significant dependence of the FIR in relation to the excitation laser power density [17]. As expected, Δ parameter in all cases showed an exponential behavior as a function of temperature (see Fig. S1 in Supporting Information), well correlated with what should be expected from Eq. (3). Fig. 9 shows the logarithm plot of the Δ parameter for different excitation power densities using the same luminescent material thermometer. The data have been well fitted with the Eq. (3) in its following logarithm form: $\ln(\Delta) = \ln(B_{FIR}) + (\frac{-\Delta E_{FIR}}{k_B T})$. From the fittings we extracted B_{FIR} and ΔE_{FIR} values for each case, which are summarized in Table 1.

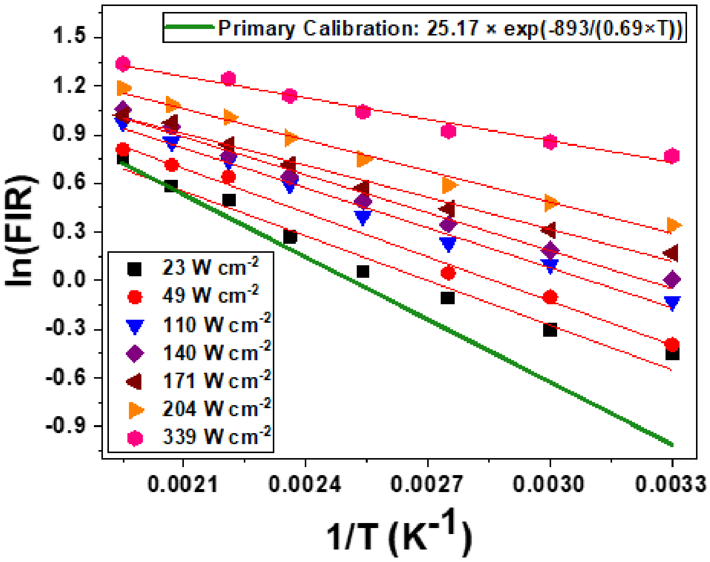

Fig. 9. Logarithmic plot of FIR for 1 at.% Er^{3+}, 20 at.% Yb^{3+}: $GdVO_4$ MCs as a function of the inverse of temperature and the corresponding fitting according to the Boltzmann distribution law described in its logarithm form ($\ln(\Delta) = \ln(B) + (\frac{-\Delta E}{k_B T})$). The green line represents the primary calibration.

The dependence of ΔE_{FIR} with the excitation laser powers for the analysed MCs is depicted in Fig. 4 and the obtained values are summarized in Table 1. The values fall in the 306-637 cm^{-1} range. It is remarkable that the fitted energy gap values decrease faster by increasing the excitation laser power. This evidence that the dependence of the intensity ratio with the temperature deviates from the Boltzmann distribution law when the excitation laser power increased. It can be seen in figure 9, as slope $\Delta E_{FIR}/K$, decreases in the linear relationship between the thermometric parameter, $ln\Delta$, and the inverse of temperature, $1/T$. As already previously reported by several authors [18,34] the higher δE (defined as $\delta E = (\Delta E - \Delta E_{FIR}) \times 100 / \Delta E$ and representing the percentage of difference in the fitted energy gap, ΔE_{FIR}, from the calculated one by fitting the multi-peak structure of the emission spectrum recorded at 303 K, ΔE), the lesser the Boltzmann law can model correctly the dependence of FIR with temperature. A large value of δE can be related to the increasing importance of the non-radiative processes, mainly multiphonon non-radiative decays, in the depopulation of the excited states, in this case, mainly $^2H_{11/2}$.

A similar decrease of the energy gap values has been reported for 10% Yb^{3+}, 1% Er^{3+}:$CaWO_4$ phosphors [36] when the temperature increased. Therefore, the increase of the excitation laser power leads to a heating effect in the sample that caused a reduction of the energy gap value when determined from the fitting procedure, which is related to the increasing role of the non-radiative processes governing the electronic population between the $^2H_{11/2}$ and $^4S_{3/2}$ levels in Er^{3+}.

Table 1
Experimental (ΔE) and FIR fitted (ΔE_{FIR}) energy gap values between the $^2H_{11/2}$ and $^4S_{3/2}$ thermally coupled levels of Er^{3+}, B_{FIR} pre-exponential constant determined from the fitted FIR curves, and thermometric parameters (thermal sensitivities and temperature uncertainties) determined for 1 at.% Er^{3+}, 20 at.% Yb^{3+}: $GdVO_4$ MCs operated under UC conditions (980 nm) at various excitation laser power densities (0-339 W cm^{-2}) in the 299.9-513 K temperature range.

Excitation laser power density (W cm^{-2})	**ΔE' (cm^{-1})**	**ΔE_{FIR} (cm^{-1})**	**δE (%)**	**B_{FIR}**	**$S_{r\max}$ (using ΔE_{FIR}) (%K^{-1})**	**$\delta T_{\min}$ (using ΔE_{FIR}) (K)**	**$S_{a\max}$ (using ΔE_{FIR}) (10^{-3}K^{-1})**
Zero Limit	-	-		25.17	1.427*	0.350*	4.960* at T_0=299.9 K
23	869	637	27%	11.90	0.998	0.500	7.421 at 513 K
49	852	630	26%	13.37	0.986	0.506	8.382 at 453 K
110	851	569	33%	12.63	0.891	0.560	8.364 at 453 K
140	848	540	36%	12.41	0.846	0.590	8.621 at 483 K
171	850	455	46%	9.82	0.713	0.700	8.463 at 303 K
204	851	444	48%	11.04	0.695	0.719	9.789 at 303 K
339	851	306	64%	8.89	0.479	1.042	10.372 at 303 K

* Thermometric performances calculated at T_0 =299.9 K.

3.5. Dependence of the relative and absolute thermal sensitivities and thermal resolution with excitation power density

The figures of merit usually used to compare the performance of the thermometers, independently of their nature, are the absolute and relative thermal sensitivities, S_a and S_r, respectively, and the temperature resolution, δT [1,37]. The relative thermal sensitivity of our MCs excited at different excitation laser power densities is calculated by [37]:

$$S_r = 100 \times \left|\frac{1}{\Delta}\frac{\partial \Delta}{\partial T}\right| = 100 \times \frac{\Delta E}{k_B T^2} \qquad (6)$$

Whereas, the absolute thermal sensitivity can be determined from [37]:

$$S_a = \frac{\partial \Delta}{\partial T} = \Delta \frac{\Delta E}{k_B T^2} \qquad (7)$$

The temperature resolution can be determined from the sensitivity of the detection system and the calculated relative thermal sensitivity, according to the following equation [38]:

$$\delta T = \frac{1}{S_r}\frac{\delta \Delta}{\Delta} \qquad (8)$$

where $\delta\Delta/\Delta$ is the sensitivity related to the detection system used, in our case of 0.5% [39].

Using the ΔE_{FIR} values obtained from the linear fit of the logarithm plot of FIR as a function of the reciprocal absolute temperature shown in Fig. 8; and Eq. (6), (7) and (8), the relative and absolute sensitivities and the temperature resolution for the analyzed sample have been calculated in the 303-513 K temperature range and at the 23 to 339 W cm^{-2} range of excitation laser power densities (see Fig. 10). For the Er^{3+},Yb^{3+}: GdVO$_4$ MCs, it can be seen that S_r decreases as the temperature and the excitation laser power density values increases, while δT increases. At low excitation laser power densities, S_a increases as the temperature increases. With increasing gradually, the excitation power, the S_a variation tendency as a function of temperature is progressively reversed to approach a decreasing path with increasing temperature. From the excitation power density separating the saturated and the non-saturated regimes (171 W cm^{-2}), the decrease rate of S_a from one temperature to another becomes greater as the excitation power density of the laser increases. So, the best relative thermal sensitivity and thermal resolution for the as-grown MCs were obtained at low temperatures (303 K) and at low excitation laser power densities (23 W cm^{-2}), reaching 0.998 %K^{-1} and 0.500 K, respectively. Whereas, the best absolute thermal sensitivity was achieved at 303 K and at 339 W cm^{-2} with a value of 10.136 10^{-3} K^{-1}.

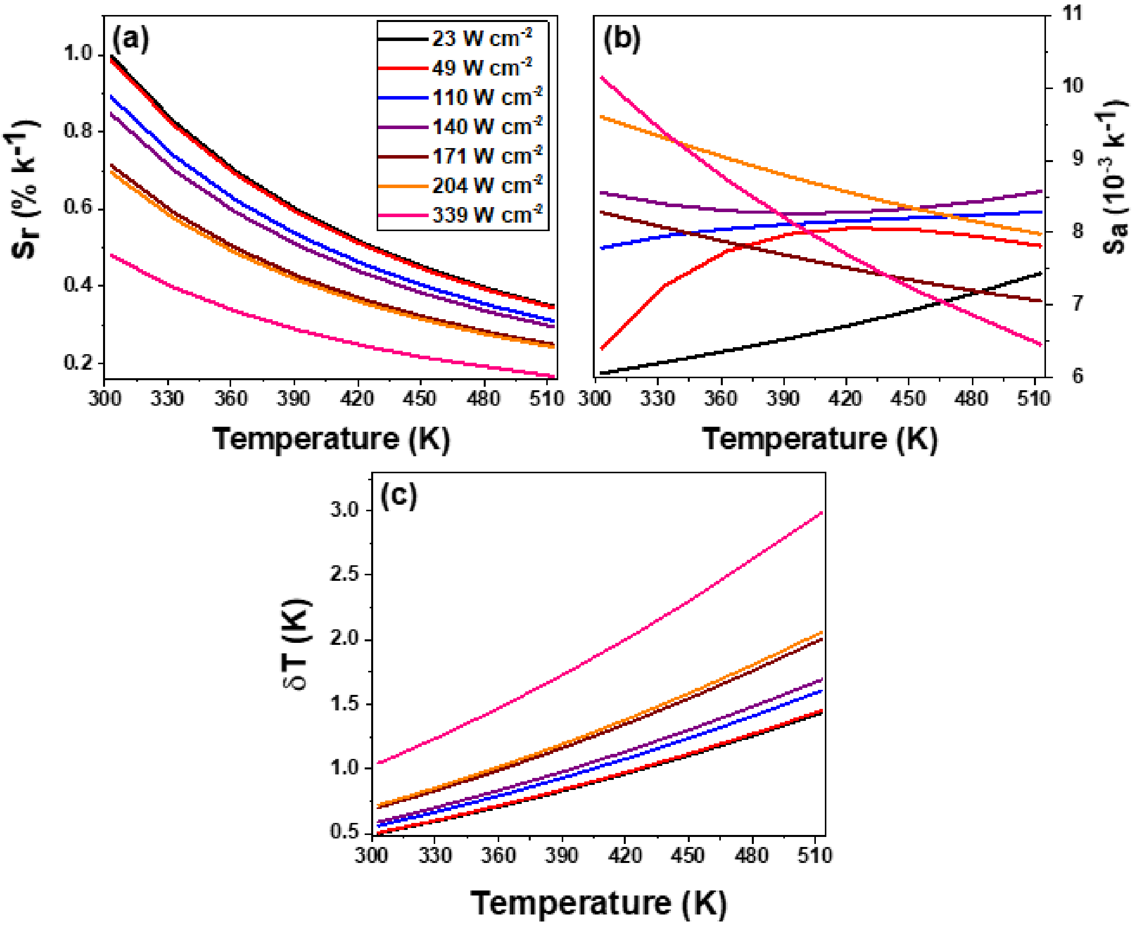

Fig. 10. Evolution of the thermometric parameters calculated for the 1 at. % Er^{3+}, 20 at.% Yb^{3+}: GdVO$_4$ sample in the 303-513 K temperature range excited under 980 nm at different excitation laser power densities: (a) relative thermal sensitivity, (b) absolute thermal sensitivity, and (c) thermal resolution.

Fig. 11 highlights the evolution of the maximum values for the relative and absolute sensitivities and the minimum values of the temperature resolution with the excitation laser power density for the sample analyzed under 980 nm laser excitation in the temperature range 303-513 K, considering as ultimate values those in the limit of zero excitation laser power density. These values are also listed in Table 1.

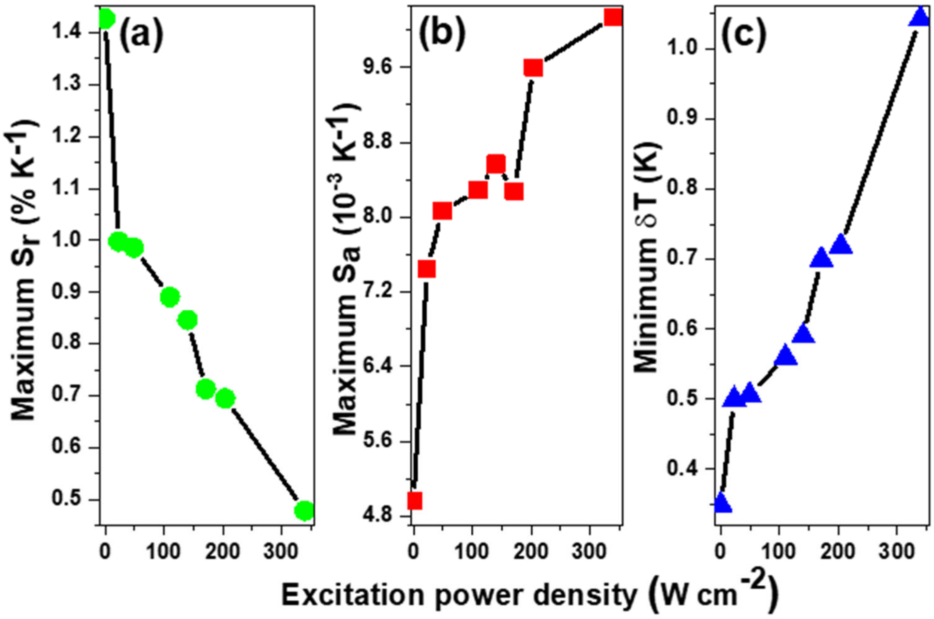

Fig. 11. Excitation laser power density dependence of the thermometric parameters for the 1 at. % Er^{3+}, 20 at. % Yb^{3+}: $GdVO_4$ MCs operated under a UC process excited at 980 nm in the 303-513 K temperature range: (a) maximum values for the relative thermal sensitivity, (b) maximum values for the absolute thermal sensitivity, and (c) minimum values for the temperature resolution. The first data in all figures were determined in the limit of zero excitation laser power density with $\Delta_0 = 0.35$, $\Delta E = 893$ cm^{-1}, and $T_0 = 299.9$ K.

From Fig. 11, it can be seen that the relative sensitivity for the sample decreases gradually with the increase of the excitation laser power density, from its maximum value of 1.427 % K^{-1} at the limit of zero excitation laser power density to 0.479 % K^{-1} at 339 W cm^{-2}. A similar behavior has been reported in 1 at. % Er, 5 at. % Yb: $BaMoO_4$ MCs [17] and in 0.1 at. % Er: $LiYbP_4O_{12}$ nanocrystals [27]. As discussed by Xin *et al.* [17], even a small increasing in temperature can affect Δ that keeps behaving strictly as the Boltzmann distribution law benefiting a high sensing sensitivity at low excitation laser power densities, and in this case, there are low electronic populations of the $^2H_{11/2}$ and $^4S_{3/2}$ levels. Whereas, the absolute sensitivity and the thermal resolution increase gradually with the increase of the excitation laser power density, respectively, from 4.96 10^{-3}K^{-1} and 0.35 K, respectively, at the limit of zero excitation laser power density to 10.136 10^{-3}K^{-1} and 1.042 K, respectively, at 339 W cm^{-2}. So, better values of the relative thermal sensitivity and the thermal resolution were observed at the limit of zero excitation laser power density, while, a better absolute sensitivity was obtained at higher excitation laser power densities (339 W cm^{-2}). These results reveal that the excitation power density affects substantially the temperature sensing performance of the analyzed sample. Also, we can extract the conclusion that a secondary thermometer will only behave similarly than the primary thermometer when working at low excitation laser power densities. In our case, the limit is 23 W cm^{-2}.

Using the thermometric parameter values, S_r and δT, obtained in the limit of zero excitation laser power density and at $T_0 = 299.9$, the error at this temperature can be calculated, respectively, by the expressions below [40]:

$$\delta S_r = S_r\sqrt{\left(\frac{\varepsilon\Delta E}{\Delta E}\right)^2 + \left(-2\frac{\theta T}{T}\right)^2} \qquad (9)$$

$$\sigma_{\delta T} = \delta T\frac{\delta S_r}{S_r} \qquad (10)$$

where $\varepsilon\Delta E$ = 6 cm^{-1} represents the error in the determination of the fitted energy gap (ΔE = 893 cm^{-1}) and it was given by the experimental fit data, θT = 0.1 K is the uncertainty in the measured temperature given by the heating stage manufacturer, and $T = T_0$ = 299.9 K corresponds to the temperature of the sample with no laser-induced heating. The calculated values for these thermometric parameters with their errors are 1.427 ± 0.009 % K^{-1} and 0.350 ± 0.002 K, respectively. In the limit of zero excitation laser power density, the errors in the thermometric parameters are insignificant.

The variation of the relative thermal sensitivity and the thermal resolution considering that the laser does not introduce any extra heating on the sample (it means by using ΔE = 893 cm^{-1} and $\Delta = \Delta_0$ = 0.35) in the 303-513K temperature range are reported in Fig. 12. They are also compared to the ones affected by laser heating and measured at 23 W cm^{-2} studied in the same range of temperatures and for the same sample (see Fig. 12). It is worth noting that under both conditions, S_r decreases as the temperature increases, while the thermal resolution increases as the temperature increases. However, the results obtained at the limit of zero excitation laser power density remain always better than those obtained under applying an excitation laser power density of 23 W cm^{-2}. When the temperature increases, the difference in the relative thermal sensitivity between the one obtained when the sample was excited at the limit of zero excitation laser power density and the one obtained when the sample was excited at 23 W cm^{-2} decreases from 0.401 % K^{-1} at 303 K to 0.139 % K^{-1} at 513 K. However, the difference in the temperature resolution follows the inverse trend, and it increases when the temperature increases from 0.1 K at 303 K to 0.4 K at 513 K. It is quite appreciable that the temperature detection sensor developed in this work is more efficient, as much as the temperature of the sample and the excitation laser power density are lower, i.e. when there is no extra-heating of the sample by laser excitation.

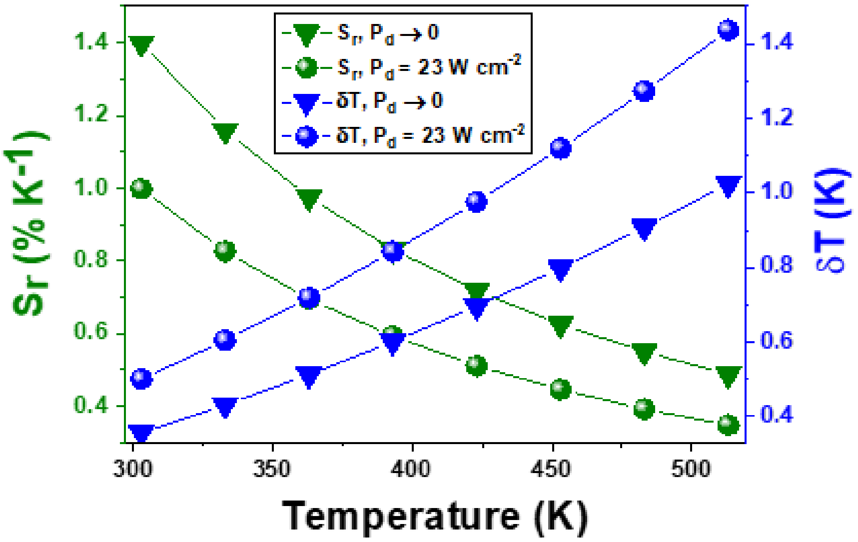

Fig. 12. Comparison between the thermometric parameters (thermal sensitivities and thermal resolutions) obtained under two different conditions of excitation laser power densities for the 1 at. % Er^{3+}, 20 at. % Yb^{3+}: GdVO$_4$ MCs analyzed in the 303-513 K temperature range. Triangles represent the data obtained at the limit of zero excitation laser power density, I→0. Spheres represent the data obtained at an excitation power density of 23 W cm^{-2}.

4. Conclusions

In summary, the performance of a luminescent primary thermometer based on Er^{3+},Yb^{3+}: GdVO$_4$ MCs has been demonstrated using the Boltzmann distribution equation of state that governs the electronic population between the two thermally couple levels, $^2H_{11/2}$ and $^4S_{3/2}$, of Er^{3+} ions. ~~It has been shown that for a primary thermometer, the thermal luminescence sensor based on Er^{3+},Yb^{3+}: GdVO$_4$ MCs should be working at low excitation laser power densities, in order to avoid as much as possible the~~

~~extra heating of the sample induced by the laser excitation.~~ For high excitation density, the local temperature of the thermometer increases and this temperature increment can be probed by the luminescence primary thermometer. The secondary thermometer is based on the temperature dependence of a ratio of intensities involving one emission intensity that is thermally quenched and another one that is thermally enhanced. The critical advantage of the secondary thermometer is to be more sensitive than the primary. When acting as a secondary thermometer, the effect of the excitation laser power density on the luminescence thermometric ratio based on the integrated intensities of the emissions in the green arising from the Er^{3+} ions has been analyzed. The secondary thermometer will only behave similarly than the primary thermometer when working at low excitation laser power densities.

Acknowledgements

This work was supported by the Spanish Government under projects MAT2016-75716-C2-1-R (AEI/FEDER, UE) and by the Generalitat de Catalunya under project 2017SGR755.

References

[1] C.D.S. Brites, A. Millán, L.D. Carlos, Chapter 281 - Lanthanides in Luminescent Thermometry, in: B. Jean-Claude, P. Vitalij K. (Eds.), Handb. Phys. Chem. Rare Earths, Elsevier, 2016: pp. 339–427. https://doi.org/10.1016/bs.hpcre.2016.03.005.

[2] L. Labrador-Páez, M. Pedroni, A. Speghini, J. García-Solé, P. Haro-González, D. Jaque, Reliability of rare-earth-doped infrared luminescent nanothermometers, Nanoscale. 10 (2018) 22319–22328. https://doi.org/10.1039/C8NR07566B.

[3] S. A. Wade, S. F. Collins, G. W. Baxter, Fluorescence intensity ratio technique for optical fiber point temperature sensing, J. Appl. Phys. 94 (2003) 4743–4756. https://doi.org/10.1063/1.1606526.

[4] M.D. Dramićanin, Sensing temperature via downshifting emissions of lanthanide-doped metal oxides and salts. A review, Methods Appl. Fluoresc. 4 (2016) 042001. https://doi.org/10.1088/2050-6120/4/4/042001.

[5] A.H. Khalid, K. Kontis, 2D surface thermal imaging using rise-time analysis from laser-induced luminescence phosphor thermometry, Meas. Sci. Technol. 20 (2009) 025305. https://doi.org/10.1088/0957-0233/20/2/025305.

[6] S. Balabhadra, M. L. Debasu, C.D.S. Brites, R. A. S. Ferreira, L. D. Carlos, Upconverting nanoparticles working as primary thermometers in different media, J. Phys. Chem. C. 121 (2017) 13962–13968. https://doi.org/10.1021/acs.jpcc.7b04827.

[7] C. D. S. Brites, E. D. Martínez, R. R. Urbano, C. Rettori, L.D. Carlos, Self-Calibrated double luminescent thermometers through Upconverting nanoparticles Frontiers in Chemistry, 7 (2019) Article 267. doi: 10.3389/fchem.2019.00267

[8] E. D. Martínez, C. D. S. Brites, L. D. Carlos, A. F. García-Flores, R. R. Urbano, C. Rettori, Electrochromic switch devices mixing small- and large-Sized upconverting Nanocrystals, Adv. Funct. Mater. 29 (2019) 1807758. https://doi.org/10.1002/adfm.201807758.

[9] M. Suta, A. Meijerink, A theoretical framework for ratiometric single ion luminescent thermometers—thermodynamic and kinetic guidelines for optimized performance, Adv. Theory Simul. 3 (2020) 3, 2000176. doi: 10.1002/adts.202000176

[10] S. Balabhadra, M. L. Debasu, C. D .S. Brites, L.A.O. Nunes, O.L. Malta, J. Rocha, M. Bettinelli, L. D. Carlos, Boosting the sensitivity of Nd^{3+}-based luminescent nanothermometers, Nanoscale. 7 (2015) 17261–17267. https://doi.org/10.1039/C5NR05631D.

[11] M. T. Carlson, A. Khan, H. H. Richardson, Local temperature determination of optically excited nanoparticles and nanodots, Nano Lett. 11 (2011) 1061–1069. https://doi.org/10.1021/nl103938u.

[12] M. L. Debasu, D. Ananias, I. Pastoriza-Santos, L. M. Liz-Marzán, J. Rocha, L.D. Carlos, All-in-one optical heater-thermometer nanoplatform operative from 300 to 2000 K based on Er^{3+} emission and blackbody radiation, Adv. Mater. 25 (2013) 4868–4874. https://doi.org/10.1002/adma.201300892.

[13] A. M. P. Botas, C .D. S. Brites, J. Wu, U. Kortshagen, R. N. Pereira, L. D. Carlos, R. A. S. Ferreira, A new generation of primary luminescent thermometers based on Silicon

nanoparticles and operating in different media. Part. Part. Syst. Charact. 33 (2016)740–748. DOI: 10.1002/ppsc.201600198

[14] B. del Rosal, D. Jaque, Upconversion nanoparticles for in vivo applications: limitations and future perspectives, Methods Appl. Fluoresc. 7 (2019) 022001. https://doi.org/10.1088/2050-6120/ab029f.

[15] S. Sinha, M.K. Mahata, K. Kumar, Enhancing the upconversion luminescence properties of Er^{3+}–Yb^{3+} doped yttrium molybdate through Mg^{2+} incorporation: effect of laser excitation power on temperature sensing and heat generation, New J. Chem. 43 (2019) 5960–5971. https://doi.org/10.1039/C9NJ00760A.

[16] L. Li, L. Zheng, W. Xu, Z. Liang, Y. Zhou, Z. Zhang, W. Cao, Optical thermometry based on the red upconversion fluorescence of Er^{3+} in $CaWO_4$:Yb^{3+}/Er^{3+} polycrystalline powder, Opt. Lett. 41 (2016) 1458–1461. https://doi.org/10.1364/OL.41.001458.

[17] X. Liu, R. Lei, F. Huang, D. Deng, H. Wang, S. Zhao, S. Xu, Dependence of upconversion emission and optical temperature sensing behavior on excitation power in Er^{3+}/Yb^{3+} co-doped $BaMoO_4$ phosphors, J. Lumin. 210 (2019) 119–127. https://doi.org/10.1016/j.jlumin.2019.01.065.

[18] N.M. Bhiri, M. Dammak, M. Aguiló, F. Díaz, J.J. Carvajal, M.C. Pujol, Stokes and anti-Stokes operating conditions dependent luminescence thermometric performance of Er^{3+-}doped and Er^{3+}, Yb^{3+} co-doped $GdVO_4$ microparticles in the non-saturation regime, J. Alloys Compd. 814 (2020) 152197. https://doi.org/10.1016/j.jallcom.2019.152197.

[19] M.G. Nikolić, D.J. Jovanović, M.D. Dramićanin, Temperature dependence of emission and lifetime in Eu^{3+}- and Dy^{3+}-doped $GdVO_4$, Appl. Opt. 52 (2013) 1716–1724. https://doi.org/10.1364/AO.52.001716.

[20] R. Calderón-Villajos, C. Zaldo, C. Cascales, Enhanced upconversion multicolor and white light luminescence in SiO_2-coated lanthanide-doped $GdVO_4$ hydrothermal nanocrystals, Nanotechnology. 23 (2012) 505205. https://doi.org/10.1088/0957-4484/23/50/505205.

[21] N. Zhang, J. Wang, X. Hu, H. Zhang, C.C. Santos, A.P. Ayala, I. Guedes, Phonons in isostructural (Nd,Yb):$YxGd_{1-x}(VO_4)$ laser crystals: A Raman scattering study, J. Solid State Chem. 184 (2011) 905–910. https://doi.org/10.1016/j.jssc.2011.02.018.

[22] S. Thakur, A.K. Gathania, Synthesis and characterization of YVO_4-based phosphor doped with Eu^{3+} ions for display devices, J. Electron. Mater. 44 (2015) 3444–3449. https://doi.org/10.1007/s11664-015-3884-4.

[23] R. T. Harley, W. Hayes, S. R. P. Smith, Raman study of phase transitions in rare earth vanadates, Solid State Commun. 9 (1971) 515–517. https://doi.org/10.1016/0038-1098(71)90136-0.

[24] K. Lenczewska, M. Stefanski, D. Hreniak, Synthesis, structure and NIR luminescence properties of Yb^{3+} and Bi^{3+}-activated vanadate $GdVO_4$, J. Rare Earths. 34 (2016) 837–842. https://doi.org/10.1016/S1002-0721(16)60103-5.

[25] J. F. Suyver, J. Grimm, M. K. van Veen, D. Biner, K.W. Krämer, H.U. Güdel, Upconversion spectroscopy and properties of $NaYF_4$ doped with Er^{3+}, Tm^{3+} and/or Yb^{3+}, J. Lumin. 117 (2006) 1–12. https://doi.org/10.1016/j.jlumin.2005.03.011.

[26] S. P. S. Porto, J. F. Scott, Raman Spectra of $CaWO_4$, $SrWO_4$, $CaMoO_4$, and $SrMoO_4$, Phys. Rev. 157 (1967) 716–719. https://doi.org/10.1103/PhysRev.157.716.

[27] L. Marciniak, K. Waszniewska, A. Bednarkiewicz, D. Hreniak, W. Strek, Sensitivity of a nanocrystalline luminescent thermometer in high and low excitation density regimes, J. Phys. Chem. C. 120 (2016) 8877–8882. https://doi.org/10.1021/acs.jpcc.6b01636.

[28] N. F. Zhuang, X. L. Hu, S. K. Gao, B. Zhao, J. L. Chen, J. Z. Chen, Spectral properties and energy transfer of Yb, Er:$GdVO_4$ crystal, Appl. Phys. B. 82 (2006) 607–613. https://doi.org/10.1007/s00340-005-2091-z.

[29] A. D. Pickel, A. Teitelboim, E. M. Chan, N. J. Borys, P. J. Schuck, C. Dames, Apparent self-heating of individual upconverting nanoparticle thermometers, Nat. Commun. 9 (2018) 4907. https://doi.org/10.1038/s41467-018-07361-0.

[30] C. D. S. Brites, S. Balabhadra, L. D. Carlos, Lanthanide-Based thermometers: at the cutting-edge of luminescence thermometry, Adv. Opt. Mater. 7 (2019) 1801239. https://doi.org/10.1002/adom.201801239.

[31] L. Li, F. Qin, Y. Zhou, Z. Zhang, Comprehensivestudy on the combined effect of laser-induced heating and laser power dependence on luminescence ratiometric thermometry, ACS Omega. 4 (2019) 3646–3652. https://doi.org/10.1021/acsomega.8b02974.

[32] R.E. Joseph, D. Busko, D. Hudry, G. Gao, D. Biner, K. Krämer, A. Turshatov, B. S. Richards, I.A. Howard, A method for correcting the excitation power density dependence of upconversion emission due to laser-induced heating, Opt. Mater. 82 (2018) 65–70. https://doi.org/10.1016/j.optmat.2018.05.025.

[33] M. Pollnau, D.R. Gamelin, S.R. Lüthi, H.U. Güdel, M.P. Hehlen, Power dependence of upconversion luminescence in lanthanide and transition-metal-ion systems, Phys. Rev. B. 61 (2000) 3337–3346. https://doi.org/10.1103/PhysRevB.61.3337.

[34 H. M. Noh, H.K. Yang, B. K. Moon, B.C. Choi, J. H. Jeong, H. Choi, J. H. Kim, Effect of Yb^{3+} Concentrations on the upconversion luminescence properties of ZrO_2:Er^{3+},Yb^{3+} phosphors, Jpn. J. Appl. Phys. 52 (2013) 01AM02. https://doi.org/10.7567/JJAP.52.01AM02.

[35] X. Wang, Q. Liu, Y. Bu, C.-S. Liu, T. Liu, X. Yan, Optical temperature sensing of rare-earth ion doped phosphors, RSC Adv. 5 (2015) 86219–86236. https://doi.org/10.1039/C5RA16986K.

[36] L. Li, F. Qin, Y. Zhou, Y. Zheng, H. Zhao, Z. Zhang, Influence of the multiphonon non-radiative relaxation on the luminescence ratiometric thermometry, J. Phys. Appl. Phys. 51 (2018) 245103. https://doi.org/10.1088/1361-6463/aac162.

[37] C. D. S. Brites, P. P. Lima, N. J. O. Silva, A. Millán, V. S. Amaral, F. Palacio, L. D. Carlos, Thermometry at the nanoscale, Nanoscale 4 (2012) 4799–4829. https://doi.org/10.1039/C2NR30663H.

[38] Z. Wang, D. Ananias, A. Carné-Sánchez, C. D. S. Brites, I. Imaz, D. Maspoch, J. Rocha, L. D. Carlos, Lanthanide–Organic framework nanothermometers prepared by spray-drying, Adv. Funct. Mater. 25 (2015) 2824–2830. https://doi.org/10.1002/adfm.201500518.

[39] O. A. Savchuk, J. J. Carvajal, C.D. S. Brites, L. D. Carlos, M. Aguilo, F. Diaz, Upconversion thermometry: a new tool to measure the thermal resistance of nanoparticles, Nanoscale. 10 (2018) 6602–6610. https://doi.org/10.1039/C7NR08758F.

[40] J.-C.G. Bünzli, Chapter 287 - Lanthanide Luminescence: From a mystery to rationalization, understanding, and applications, in: J.-C.G. Bünzli, V.K. Pecharsky (Eds.), Handb. Phys. Chem. Rare Earths, Elsevier, 2016: pp. 141–176. https://doi.org/10.1016/bs.hpcre.2016.08.003.